remote sensing

MDPI

Article

Development of a Background Filtering Algorithm to Improve the Accuracy of Determining Underground Cavities Using Multi-Channel Ground-Penetrating Radar and Deep Learning

Dae Wook Park [1], Han Eung Kim [2], Kicheol Lee [3] and Jeongjun Park [4,*]

[1] Department of Civil Engineering, Kunsan National University, 558 Daehak-ro, Gunsan-si 54150, Republic of Korea; dpark@kunsan.ac.kr
[2] Geotechnical Korea Engineering Co., Ltd., 91 LS-ro, Dongan-gu, Anyang-si 14119, Republic of Korea; he-kim@gk-eng.co.kr
[3] Corporate Affiliated Research Institute, UCI Tech, 313 Inha-ro, Michuhol-gu, Incheon 22012, Republic of Korea; leeki3539@gmail.com
[4] Incheon Disaster Prevention Research Center, Incheon National University, 119 Academy-ro, Yeonsu-gu, Incheon 22012, Republic of Korea
* Correspondence: jjpark72@inu.ac.kr; Tel.: +82-10-4722-2971

Abstract: In the process of using multi-channel ground-penetrating radar (GPR) for underground cavity exploration, the acquired 3D data include reflection data from underground cavities or various underground objects (structures). Reflection data from unspecified structures can interfere with the identification process of underground cavities. This study aims to identify underground cavities using a C-GAN model with an applied ResBlock technique. This deep learning model demonstrates excellent performance in the image domain and can automatically classify the presence of cavities by analyzing 3D GPR data, including reflection waveforms (A-scan), cross-sectional views (B-scan), and plan views (C-scan) measured from the ground under roads. To maximize the performance of the C-GAN model, a background filtering algorithm (BFA) was developed and applied to enhance the visibility and clarity of underground cavities. To verify the performance of the developed BFA, 3D data collected from roads in Seoul, Republic of Korea, using 3D GPR equipment were transformed, and the C-GAN model was applied. As a result, it was confirmed that the recall, an indicator of cavity prediction, improved by approximately 1.15 times compared to when the BFA was not applied. This signifies the verification of the effectiveness of the BFA. This study developed a special algorithm to distinguish underground cavities. This means that in the future, not only the advancement of separate equipment and systems but also the development of specific algorithms can contribute to the cavity exploration process.

Keywords: GPR; underground cavity; 3D data; C-GAN; BFA

check for updates

Citation: Park, D.W.; Kim, H.E.; Lee, K.; Park, J. Development of a Background Filtering Algorithm to Improve the Accuracy of Determining Underground Cavities Using Multi-Channel Ground-Penetrating Radar and Deep Learning. *Remote Sens.* **2024**, *16*, 3454. https://doi.org/10.3390/rs16183454

Academic Editor: Henrique Lorenzo

Received: 1 August 2024
Revised: 2 September 2024
Accepted: 16 September 2024
Published: 18 September 2024

Copyright: © 2024 by the authors. Licensee MDPI, Basel, Switzerland. This article is an open access article distributed under the terms and conditions of the Creative Commons Attribution (CC BY) license (https://creativecommons.org/licenses/by/4.0/).

1. Introduction

With the increase in aging infrastructure, redevelopment projects are being actively discussed, particularly in urban areas. However, due to the saturation of above-ground spaces, there are limitations to new and redevelopment projects. This has led to the active development of underground spaces, but the frequency of underground cavities is rapidly increasing. Ground subsidence resulting from these cavities is one of the most severe disasters that can occur in urban areas.

Underground cavities are formed due to changes in groundwater extraction and drainage patterns, damage to water supply connections, and aging sewer pipes. Since these underground cavities can appear without warning in urban areas, there is an increasing demand for early detection [1–3]. Unexpected ground subsidence can lead not only to road closures and economic losses but also to casualties [4,5].

Recently, ground-penetrating radar (GPR) has been used as a highly reliable technique and is evaluated as the most suitable technology for responding to ground subsidence [6–9]. GPR is a fully non-contact, non-destructive inspection technology that has gained popularity in the field of structural condition monitoring due to rapid scanning speed and 3D imaging capabilities [10]. GPR emits high-frequency electromagnetic waves into the ground and receives the reflected waves from underground objects or empty space. By analyzing the received signals, it is possible to identify the boundaries of these anomalies if there are changes in the electromagnetic properties, such as the relative permittivity of the medium or the composition of the soil layers [11,12]. Thus, GPR has been applied in archaeological and geological contexts for mapping underground features and has recently been expanded to derive the engineering properties of underground cavities and soil [13–17].

However, raw GPR signals are generally dominated by reflections from upper layers, such as paved roads, making analysis extremely difficult. Additionally, the complex geometry, changes in water content, and unexpected contaminants associated with urban roads make data interpretation even more challenging [18]. Additionally, the analysis of data obtained through GPR surveys requires specialized expertise due to the complexity and specificity of the equipment, necessitating the involvement of expert analysts. However, in reality, there is a significant shortage of specialized equipment and personnel. And there is no separate interpretation method for the 3D data obtained from GPR surveys, so experts must manually inspect and assess the data, relying heavily on subjective judgment and effort. As a result, there is a risk of missing signals indicating cavities if the expert's concentration wanes or subjective judgment excessively interferes. Moreover, the lengthy process from the start of the survey to the completion of the analysis poses a challenge for urgently responding to sudden road subsidence disasters [19,20].

To address these problems, neural network classifiers have been developed to detect buried utilities and solid objects in GPR images, and artificial neural networks have been introduced to detect pipe signatures in GPR images [21,22]. Also, machine learning techniques have been studied to extract amplitude and time delay features from GPR longitudinal scan images [23]. While traditional machine learning techniques have been successfully used to detect dominant or clear features in GPR signals, they are not well-suited for classifying multiple underground objects in complex urban areas. Furthermore, the manual feature extraction process is extremely difficult and cumbersome when interpreting GPR data in complex field conditions, which include measurement noise.

More recently, there has been active exploration of ground cavity detection using neural network models, including deep learning models. Studies have focused on traditional methods and deep learning approaches for GPR data detection [24], methods for predicting the permittivity of targets using deep learning models [25], and improving speed and accuracy through neural network models [26]. Additionally, there is ongoing research on verifying the performance of newly developed GPR systems [27]. In other words, new methods are continuously being explored. However, this study aims to focus on improving accuracy through data quality enhancement rather than developing a new prediction model. While this approach may not be as groundbreaking as innovative prediction technologies, it is expected to contribute to the overall advancement of ground cavity prediction models.

The deep learning used is focused on automation, incorporating automatic feature extraction, unsupervised learning for pre-training, and utilizing images directly in the training and testing process without image reconstruction. This paper describes a method for quickly and automatically detecting underground cavities using artificial intelligence cavity analysis technology. Specifically, it focuses on developing and validating an algorithm to remove noise in the direction of travel. This algorithm, known as the background filtering algorithm (BFA), combines a signal amplification filter and a local average subtraction technique to enhance the visibility and clarity of underground cavities beneath urban road pavements. The developed BFA was applied to a C-GAN (conditional generative adversarial network) model incorporating the ResBlock technique, which has shown excellent performance in the image domain. Finally, the C-GAN model was trained using 3D GPR

data obtained from urban roads. The effectiveness of the BFA was validated by comparing the data processed with and without the BFA, confirming the improvement in detecting underground cavities.

2. Automated Technique for the Detection of Underground Cavities Based on Deep Learning

The deep-learning-based technology developed for the automated detection of underground cavities can be detailed in three stages. First, an explanation of the operating principle of multi-channel GPR (ground-penetrating radar) will present the process of data acquisition and the various types of data. Next, the details of developing a basic tracking-based background filtering algorithm that can enhance the visibility of underground structures in GPR images will be explained. Finally, the C-GAN model with ResBlock techniques applied for the automatic detection of underground cavities using filtered images will be described.

2.1. Process and Principles for the Detection of Underground Cavities Using Multi-Channel GPR

Figure 1 illustrates the underground visualization process for acquiring 3D survey data using multi-channel GPR in a road site. The 3D GPR system consists of multiple transmitters and receiver antennas and a system for the acquisition of data. The transmitters emit high-frequency electromagnetic waves, and the receivers collect the returning waves. The typical frequency range of these electromagnetic waves spans from a few MHz to GHz. The appropriate frequency range should be selected based on the size and depth of the target object. Generally, high frequencies are used for shallower and smaller targets, while low frequencies are used for deeper and larger targets.

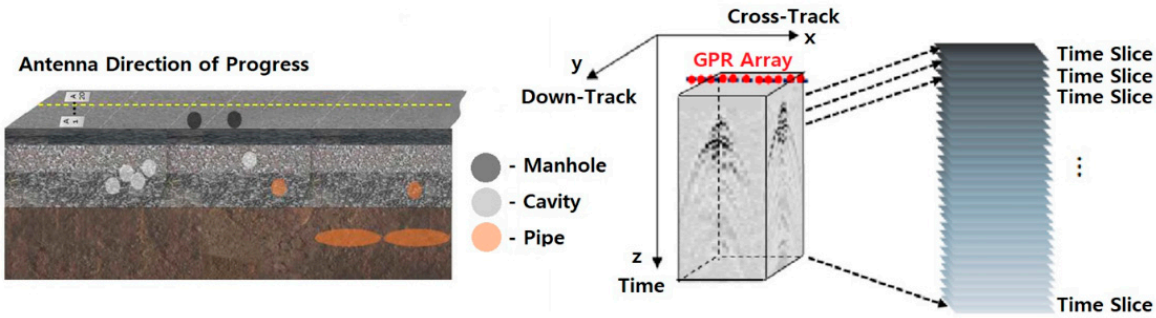


Figure 1. Schematic of data acquisition.

Multi-channel GPR typically acquires three different types of data when scanning a target area: reflection waveform (A-scan), longitudinal cross-section (B-scan), and horizontal cross-section (C-scan).

In GPR surveys, data are acquired and analyzed through three types of scans to identify cavities. First, to analyze cavity signals, the changes in signals are examined three-dimensionally (by depth variation) on planar images (C-scan). During this process, the signals are analyzed to determine whether they form a continuous linear pattern (indicating buried pipes) or an independently separated area (indicating a cavity). In the second stage, the preliminary candidate cavity images identified as independent shapes in the planar C-scan images are further analyzed in a two-dimensional B-scan cross-section. Here, strong signal intensity, phase changes, and the pattern of parabolic shapes are examined. Finally, in the third stage, considering the significant difference in dielectric constants between air and the surrounding medium, the A-scan data of the survey points are analyzed. Additional analyses of waveform phase changes, amplitude, and signal intensity are conducted to confirm the presence of cavities.

Additionally, when there are changes in the electromagnetic properties of the scanned area, such as variations in the relative permittivity of the ground layer or the presence of anomalous objects with different properties, a portion of the electromagnetic waves is reflected back to the receiving antenna. These reflected waves are then collected by the data acquisition system and used for underground object detection. In this study, various data and parameters acquired through multi-channel GPR are comprehensively analyzed. Based on the criteria for cavity selection, the presence and characteristics of cavities are determined.

2.1.1. Images of A-Scan

The A-scan provides precise time-domain information at a specific spatial point (z-axis in Figure 1). By considering the significant difference in permittivity between air and the medium, the reflection wave exhibits a waveform that progresses from negative (-) to positive (+) amplitude when reflected from the upper low-velocity layer (pavement layer) and the lower high-velocity layer (air). Therefore, the A-scan in multi-channel GPR involves analyzing the phase changes, amplitude, signal strength, and intensity of the waveform to identify cavities. Figure 2 illustrates the A-scan waveforms for two cavities and non-cavities, such as loose gravel layers and buried pipes.

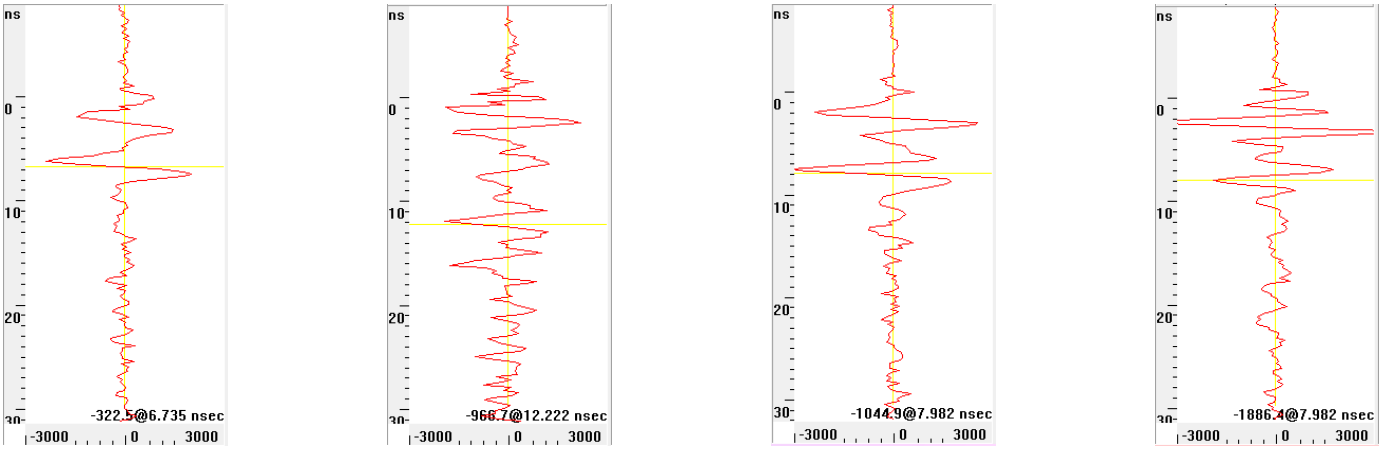
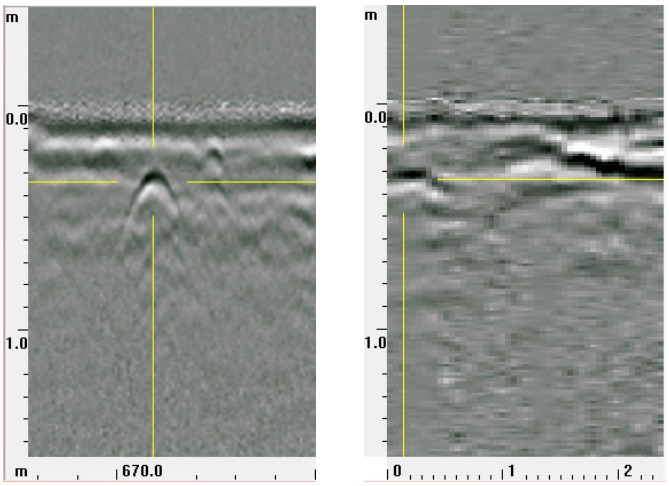


Figure 2. A-scan images: (**a**) underground cavity −1; (**b**) underground cavity −2; (**c**) loose gravel layer; (**d**) buried pipes.

2.1.2. Images of B-Scan

The B-scan in the x-z domain is comprised based on various A-scan data along the scanning path (x-axis in Figure 1). For the cavities selected by independent signal shapes in the A-scan plane image, a two-dimensional B-scan is generated, displaying longitudinal and cross-sectional images as shown in Figure 3. After, in the B-scan, the signal strength, phase changes, and patterns of parabolic shapes are analyzed and verified. Typically, boundary surfaces reflecting the received signal are represented as curves or straight lines. The boundaries of underground objects or cavities appear in a parabolic shape. The upper point of a cavity is indicated by the topmost part of the parabola formed beneath the survey point, shown as white and black sections.

Additionally, A-scan and B-scan images can be used to determine whether an underground pipe is made of metal or PVC material. In the analysis of A-scan and B-scan images, if the start of the embedded image appears as (+) or white, it indicates a metallic material, such as a cast iron or steel pipe used for gas or water lines. Conversely, if the image appears as (-) or black, it indicates a PVC material, commonly used for communication conduits.



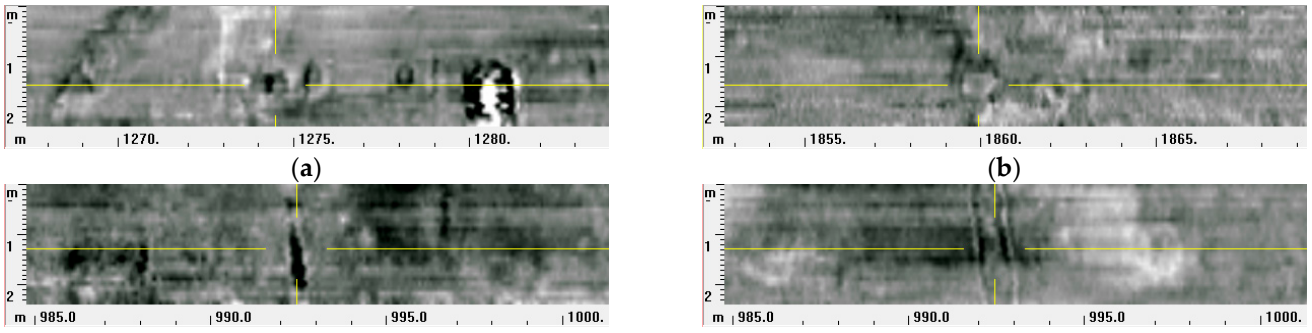
(**a**) (**b**)

Figure 3. B-scan images: (**a**) longitudinal section; (**b**) cross-section.

2.1.3. Images of C-Scan

Due to strong surface reflections, B-scan images often display dominant linear features that appear nearly straight. These surface reflections typically overwhelm underground reflections via the sudden change in permittivity from air (1 F/m^{-1}) to paved road (5 F/m^{-1}). These linear features in B-scan images can often interfere with the detection of underground objects. Therefore, B-scan images obtained using multiple antennas are combined to generate C-scan images that are visible in the x-y domain. The various C-scan images can be examined along the z-axis, representing depth, and these cross-sectional C-scan images are used to further characterize the detected features.

To analyze cavity signals, the changes in signals are examined three-dimensionally in the planar image, and shape changes with depth are confirmed. As shown in Figure 4, buried pipelines exhibit a linear pattern, while cavities form a distinct area with abrupt amplitude changes along the boundary, showing an independently separated pattern. Therefore, cavities need to be identified by comprehensively analyzing planar, longitudinal, and cross-sectional images based on the independent signal shapes.



(**a**) (**b**)

(**c**) (**d**)

Figure 4. C-scan images with depth from the ground surface: (**a**) underground cavity at a depth of 32 cm; (**b**) underground cavity at a depth of 42 cm; (**c**) buried pipes at a depth of 26 cm; (**d**) buried pipes at a depth of 36 cm.

2.2. Background Filtering Algorithm (BFA)

In this study, a filtering algorithm of noise removal was developed to enhance the visibility of underground objects by removing dominant linear features and unwanted pattern noise from B-scan images. It is a background filtering algorithm (BFA). This algorithm consists of six steps. The filtered images can significantly enhance the visibility of underground cavities and are effectively used in the subsequent process involving the

ResBlock technique applied to the C-GAN model. The workflow diagram for the BFA is illustrated in Figure 5.

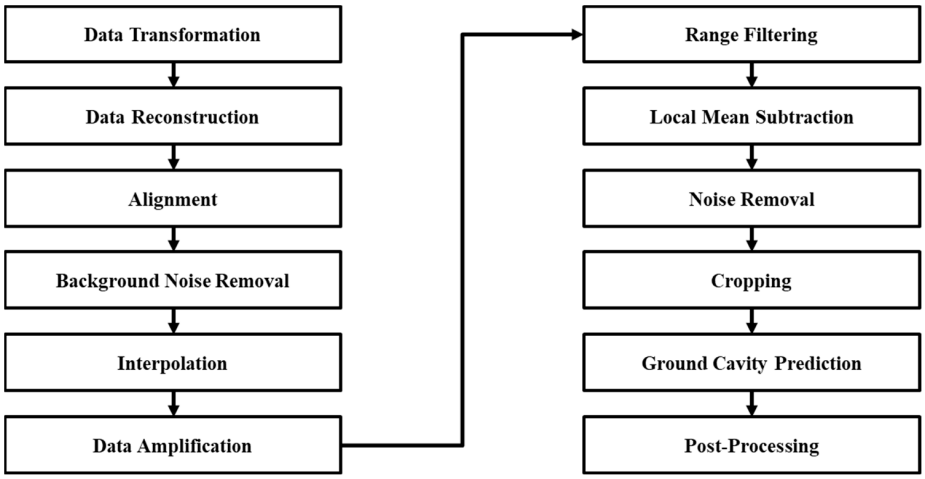


Figure 5. Workflow of the BFA.

2.2.1. Collection of 3D GPR Data

3D GPR data are collected using multi-channel antennas to receive raw data from the underground space, as illustrated in Figure 1. This setup allows for the acquisition of raw data corresponding to 25 channels, providing 25 longitudinal, planar, and cross-sectional views of the underground space. It is important to note that the measured GPR signals generally attenuate as they propagate through specific media. This attenuation must be considered during the data analysis process.

2.2.2. Conversion and Restructuring of Data

The raw data obtained from 3D GPR must be converted into a format that can be processed by deep learning models. The raw data are in an RD3 format, consisting of a combination of texts and numbers, and are not directly analyzable. Therefore, a decoding process was performed to convert these data into a one-dimensional array (1D-array) format, with numbers listed in a single column. This process utilized the Numpy library and involved converting the RD3 format raw data into the NPY format (*.npy). Subsequently, a data restructuring step was carried out to convert the one-dimensional array data in the NPY format into a three-dimensional array format, making them easier to use in deep learning applications. This conversion allows the data to be visualized and analyzed based on each antenna channel, the depth of the underground space, and the distance between the antenna and the underground cross-section.

As shown in Figure 6, the reshape function of the Numpy library was used to reconstruct the one-dimensional array data into three-dimensional array data. The three-dimensional array data consist of elements arranged as follows:

- [Antenna Channels (width of the survey vehicle)]
- [Depth of the Underground Space]
- [Distance between the Antenna and the Underground Cross-Section (distance along the survey vehicle's driving direction)]
- Etc.

```
array([[[-190, -190, -190, ...,  -59,  -18,   -4],
        [-3071, -3071, -3071, ..., -2640, -2661, -2939],
        [-9244, -9244, -9244, ..., -8670, -7999, -8983],
        ...,
        [ 988,  988,  988, ...,  881,  840,  818],
        [ 1018,  1018,  1018, ...,  983,  960,  777],
        [ 1043,  1043,  1043, ...,  1002,  909,  1257]]])
```

Figure 6. Example of reconstructing data in the form of a 3-dimensional matrix.

2.2.3. Alignment of Data

A ground alignment process is performed to correct the time differences using the maximum and minimum values of the data for each channel. In the case of a 3D GPR, the reflected waves received by the antenna with 25 channels are not received at exactly the same time, so they need to be aligned by tracking the ground surface. Specifically, as shown in Figure 7, the first alignment value is calculated as the average of the maximum and minimum values of the data for each channel, and the second alignment value is calculated as the median of the maximum and minimum values of the data for each channel. By considering the pixel point corresponding to the average of the first and second alignment values as the ground surface corresponding to the underground space, the time difference for each channel can be corrected based on this pixel point.

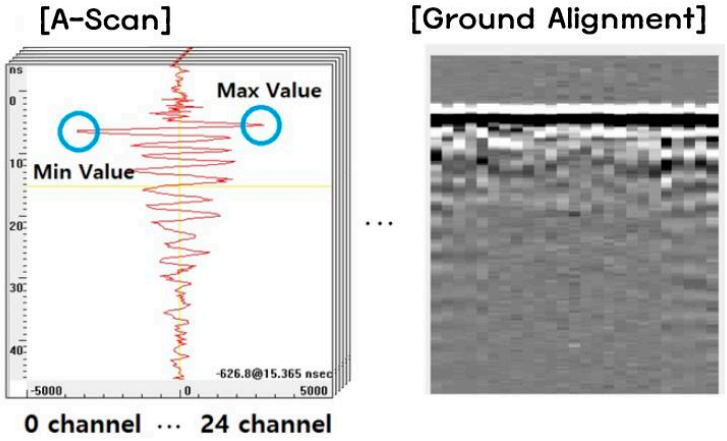


Figure 7. Process of ground alignment.

2.2.4. Background Removal and Data Interpolation

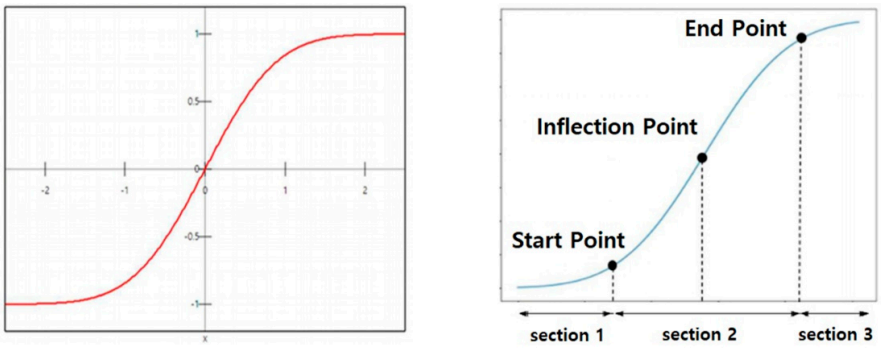
The surface portion of the data, which has undergone the data alignment process, generates strong signals unrelated to cavity signals, interfering with the detection of cavity signals. Additionally, some channels occur bias. Therefore, noise in the surface portion must be removed and bias values adjusted by subtracting the average pixel values at specific depths in the underground space. This process is known as background removal. Subsequently, data interpolation is performed. This step ensures that the data structure and format of the pre-processed data match those of the training data used for the deep learning model. The intervals between pixels in the data are adjusted to a set value.

2.2.5. Data Amplification

When the transmitted waves from the antenna pass through the boundaries of different media, reflected waves occur based on the reflectivity of the media, and only the transmitted waves continue. As the depth of the underground space increases, the strength of the transmitted waves weakens, and the strength of the reflected waves also diminishes. Consequently, signals below a specific depth become difficult to observe during the process of visualizing and analyzing the data. Previously, signal amplification was performed using linear functions or exponential functions, but this approach often resulted in excessive noise.

Therefore, this study aims to achieve an optimal data amplification appropriate for different depths in the underground space by varying the degree of amplification for the relatively shallow and relatively deep parts of the data. Specifically, a signal amplification filter, represented by a function (*erf*), is applied to the data to dynamically adjust the amplification weights for different depth intervals: the shallowest part (Zone 1), a deeper part than Zone 1 (Zone 2), and a deeper part than Zone 2 (Zone 3). The amplification filter function (*erf*) is a Sigmoid error function, as shown in Equation (1) and Figure 8a.

$$erf = \frac{2}{\sqrt{\pi}} \int_0^x e^{-t^2} dt \quad (1)$$



(**a**) (**b**)

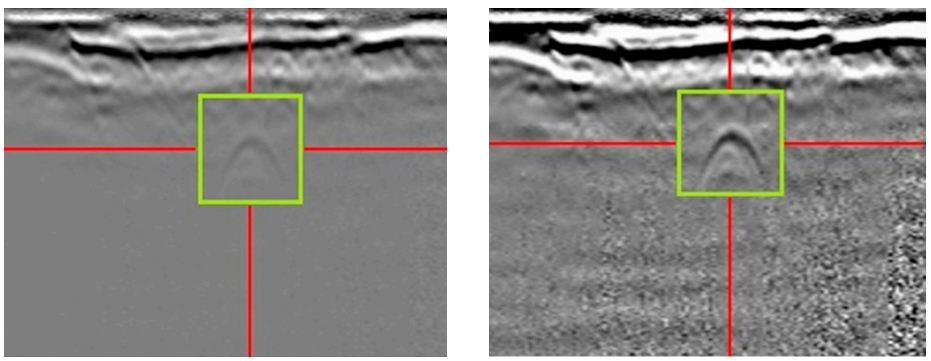
Figure 8. Data amplification function: (**a**) error function; (**b**) improved error correction function.

When applying this error function directly to amplify data with underground depth, it proved difficult to accurately detect cavities due to mismatches with the depths, widths, and sizes where cavities occur. Therefore, the error function was improved to create a new function (F), and this signal amplification filter was applied to amplify the data. Specifically, based on the error function expressed in Equation (1), additional variables were set, including the inflection range (the width between the start and end points of the inflection), the inflection midpoint (the midpoint between the start and end points), the slope of the function (*erf*) within the inflection range, and the y-axis intercept (bias) of the function (*erf*).

The final corrected error function (F) can be expressed as shown in Equation (2). Figure 8b illustrates the graph of the improved signal amplification filter function (F) based on Equation (2). Here, F represents the function of the signal amplification filter, x denotes the pixel value according to the depth of the underground space, a is the inflection midpoint (=140), b is the inflection range (=70), K is the slope of the function (F) within the inflection range (=1), C is the y-axis intercept (bias) of the function (F) (=1.5), and t is time. The x-axis represents the pixel values according to the depth of the underground space, which can be in units of pixels or cm. The y-axis represents the weight for the degree of data amplification. Additionally, the default values may vary depending on the characteristics of the underground space.

$$F = \left(erf\left(\left(\frac{x-a}{b} \right) + 1 \right) + K \right) + C \tag{2}$$

Figure 9 shows the data images before and after the application of the signal amplification filter. When the signal amplification filter is applied, it is evident that the data near the cavities are relatively more prominently amplified. This indicates that the applied improved error correction function is appropriate.



(**a**) (**b**)

Figure 9. Data images: (**a**) non-application of the improved error correction function; (**b**) application of the improved error correction function.

2.2.6. Noise Removal Using Local Average Subtraction

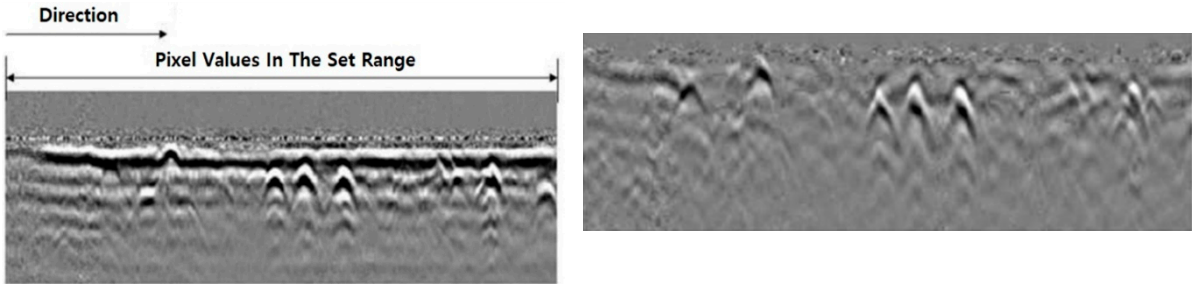
In data where errors have been corrected using traditional Kalman filters, signals that appear as straight lines in the direction of the survey vehicle's travel (e.g., pipe signals, surface signals) are not effectively removed. As a result, these straight-line signals frequently overlap with the signals from the cavity regions. This means that the cavity signals are obscured by the straight-line signals in the direction of travel.

In this study, a Gaussian function was used to remove noise in the direction of the survey vehicle's travel. However, applying a typical Gaussian filter would remove not only the noise but also the signals from the cavity regions. Therefore, in this study, instead of directly applying the Gaussian filter, a method is used in which the operation value of the Gaussian function is subtracted from the pixel value of the target pixel. This helps to selectively remove only the noise according to the driving direction of the survey vehicle.

The C-GAN model is considered the most suitable model for ground cavity prediction. The traditional deep learning method of a CNN (convolutional neural network) was initially used to extract image features for ground cavity detection. A total of 1396 image files were created and applied for training the CNN model, and 236 images were prepared for testing, resulting in an accuracy rate of 80.2%. In comparison to the C-GAN model, which achieved a 100% accuracy rate, the CNN model failed to reflect the entire dataset. Thus, the suitability of the C-GAN model for prediction after ground cavity detection was confirmed.

Figure 10 shows the data images before and after removing the straight-line noise in the direction of travel using local average subtraction. It is evident that noise near the surface and in the direction of travel, such as from pipes, is significantly reduced. Specifically, pixel values within a defined range centered on the direction of travel are selected, and the calculated value of the Gaussian function $G(x)$, expressed by Equation (3), is obtained based on the central pixel value xxx within the defined range. By subtracting this calculated value $G(x)$ from the pixel value (x), noise in the direction of travel can be removed. Here, σ is a predefined standard deviation value.

$$G(\chi) = \frac{1}{\sqrt{2\pi\sigma^2}} e^{-\frac{x^2}{2\sigma^2}} \quad (3)$$



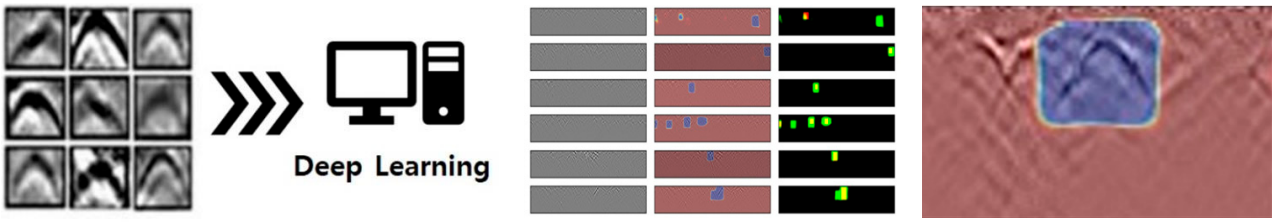
(**a**) (**b**)

Figure 10. Noise removal using local average subtraction: (**a**) non-application; (**b**) application.

2.3. C-GAN-Based Automated Underground Cavity Detection

By inputting preprocessed data into the deep learning model, it is possible to predict cavities within underground spaces. The deep learning model used in this study is a C-GAN (conditional generative adversarial network), which is an improved form of the traditional GAN. In a GAN, a generator and a discriminator compete during training, but in C-GAN, conditional data are input to obtain the desired images. There are two representative types of C-GANs: pix2pix and cycle GAN. This study uses pix2pix, which, unlike traditional GANs, inputs images instead of noise for training, and the generator learns to produce images as a result. To enhance image generation performance, the model structure employs a U-Net form, incorporating the residual block technique with skip connections to prevent vanishing gradients.

Figure 11 illustrates the data processing flow of the deep learning model utilized in this study. Figure 12 depicts the C-GAN architecture that can output cavity sections within the underground space based on pre-processed input data and pre-trained training data from 3D GPR data. Using this model eliminates the need for the reliance on expert concentration or subjective judgment in cavity surveys, allowing for real-time cavity detection and a rapid response to sudden road subsidence incidents. The predicted cavity sections in the deep learning model can be adjusted to display as images highlighted with specific colors.



(**a**) (**b**) (**c**)

Figure 11. Data processing images of the deep learning model: (**a**) input data image; (**b**) data processing; (**c**) output of the cavity section.



Figure 12. C-GAN architecture tailored for 3D GPR data classification.

3. Field Validation Tests

The deep-learning-based underground cavity automatic detection technique derived in the previous section was applied to the roads in Seoul, Republic of Korea. The validity of this technique was verified using the collected 3D GPR data.

3.1. Experimental Setup

Figure 13 shows the vehicle-type multi-channel GPR used in this field investigation. The GPR has a frequency of 400 MHz, and its effective investigation depth and width are up to 2.0 m from the surface of flexible pavement and 2.4 m, respectively. Moreover, the multi-channel GPR can perform 3-dimensional analysis; therefore, it can detect the interface of different materials and abnormal signals owing to the differences in the relative permittivity, even in identical materials. The GPR system comprises GPR antennas, a camera recording surface conditions, a global positioning system (GPS), and positioning cameras [16].

This system consists of 14 transmitting antennas and 14 receiving antennas, totaling 25 channels, and extends the survey width to 2.4 m, allowing data acquisition without survey shadow areas in a single pass. Additionally, the vehicle-based GPR survey software is divided into software for recording and controlling in the field and software for analyzing and recording data indoors. In the field, MIRA Software v.3.57.01 from MALA was used to record and control the survey equipment. For survey data analysis, a combination of MALA's rSlicer v1.0.0 and the GPRIS System developed in the Republic of Korea was utilized.

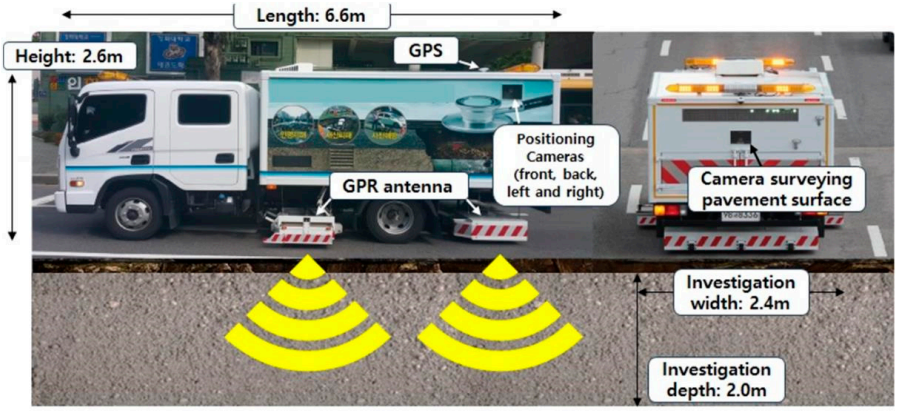


Figure 13. Field validation tests using a van with a mounted 3D GPR.

Figure 14a shows the radargram of a cross-section in the longitudinal direction from the GPR scanning, and the yellow circle represents that an underground cavity may exist. The horizontal axis indicates the distance in the longitudinal direction, and the vertical axis indicates the depth from the pavement surface. The depth from the top surface to the center of the parabolic black strip is defined as an overburden thickness measured as 0.33 m in this study. To determine the size of the cavity from the image, the boundary of the white strip above the black parabola that indicated an amplitude change in the GPR signal was set as the boundary of the cavity, and the length between the boundaries was defined as the size of the cavity. Figure 14b shows the radargram of a planar image at a depth of 0.67 m that represents the overburden thickness of the cavity.

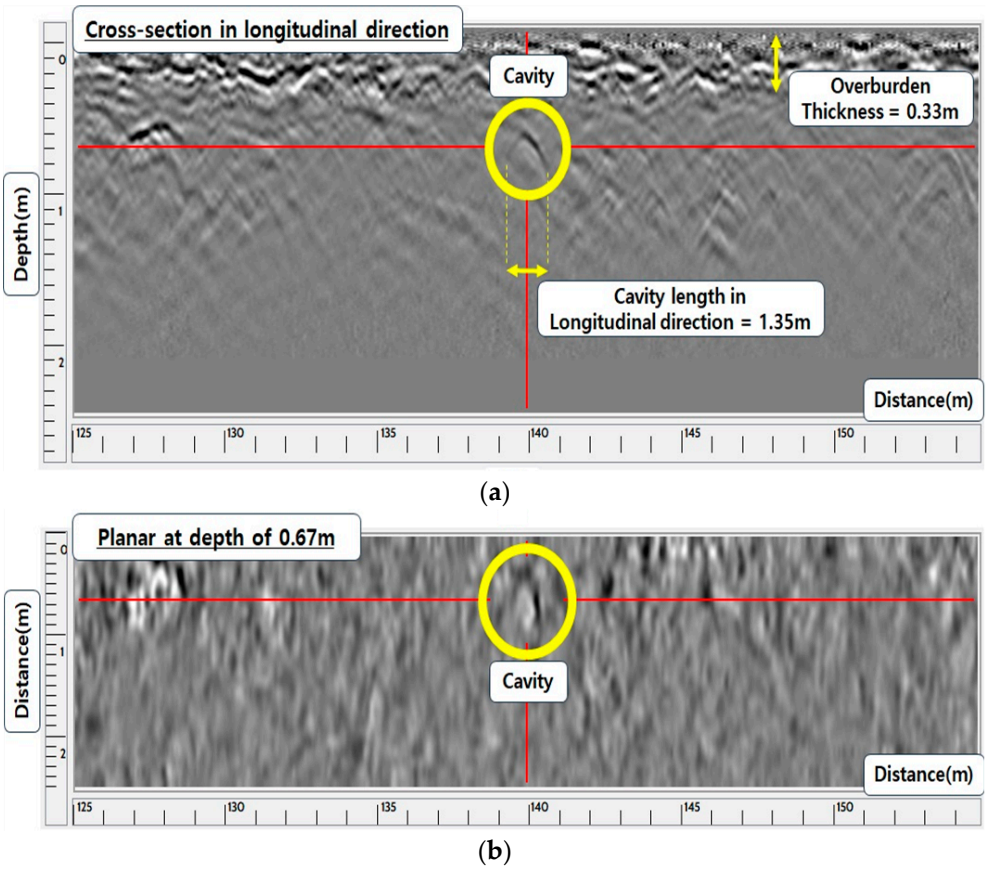
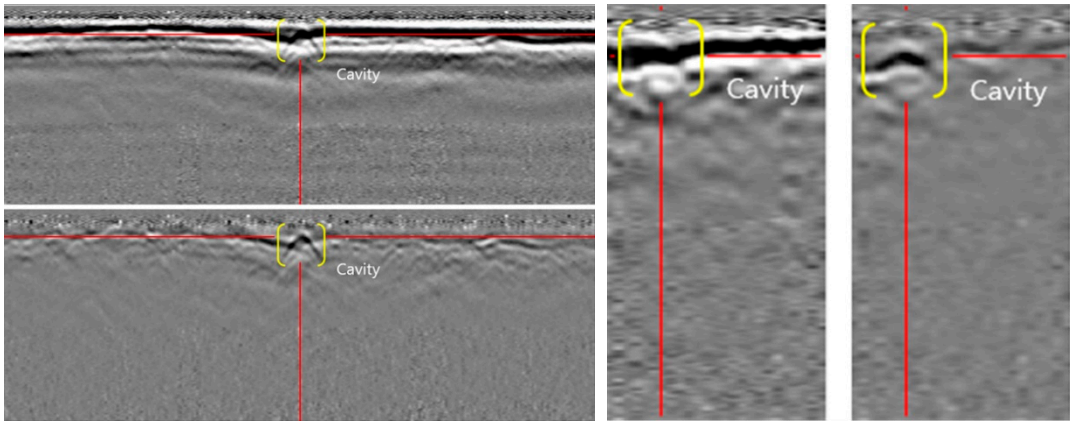


Figure 14. GPR radargrams: (**a**) cross-section in the longitudinal direction; (**b**) planar at a depth of 0.67 m.

The data in Figure 14a are non-migration data. The objective of this study is not to determine the size of the cavities but to evaluate the performance of cavity pre-processing using the BFA, making migration unnecessary in this context. Of course, during data acquisition, the apparent structure (hyperbola) reflected in the images is converted into the actual underground structure using correction methods to measure the scale of the cavity. Migration is typically used to reposition inclined surfaces to their actual underground locations and to reduce diffractions. According to the literature [16], approximately 70% of cavity waveforms detected through GPR surveys are considered to represent the actual size of the cavity, allowing for an approximate estimation of its size. However, as previously mentioned, migration is not a mandatory requirement for this study, so it was not performed.

3.2. Results of Appling the BFA

Figure 14 shows the longitudinal and cross-sectional views at locations with cavities, comparing images detected with and without the application of the BFA. In the longitudinal section, as shown in Figure 15a, the cavity appears in the form of a curve known as a parabola or hyperbola. In the upper image of Figure 15a, where the BFA is not applied, the boundary feature information of the target (underground cavity) has a weak intensity, and the geometric structure of the hyperbola is not distinct. However, in the lower image of Figure 15a, where the BFA is applied, signals that appear as black and white bands, indicating the boundary characteristics of the asphalt pavement and soil medium near the surface, are removed, making the features of the underground cavity in the longitudinal section more clearly identifiable.



(**a**) (**b**)

Figure 15. Comparison of B-Scan data with the BFA applied: (**a**) longitudinal section; (**b**) cross-section.

Similarly, the underground cavity in the cross-sectional view shown in Figure 15b also exhibits the characteristic parabolic or hyperbola curve shape. In the image on the right side of Figure 15b, where the BFA is applied, the black and white bands near the surface are removed, making the boundary of the cavity's curved shape more prominently defined.

Figure 16 shows the plan view (C-scan) at locations with cavities, comparing images with and without the application of the BFA. When examining the plan view at the same depth, it is observed that the local area is represented in black before the BFA is applied. In contrast, after applying the BFA, the black areas in the image are clearly distinguishable as underground cavities, confirming the effectiveness of the BFA in enhancing the visibility of these features.

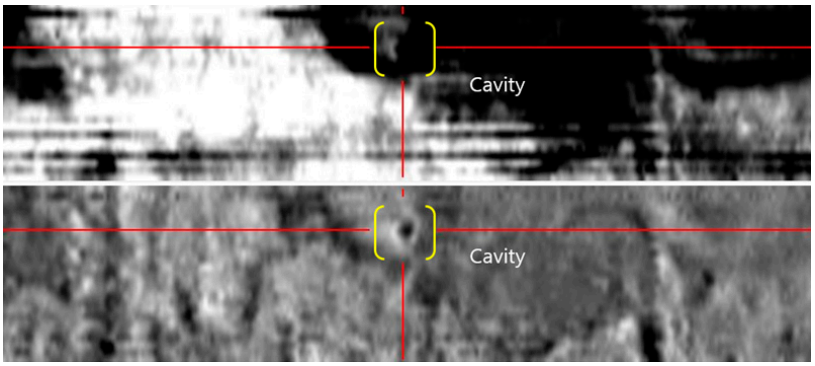


Figure 16. Comparison of plan view (C-Scan) data with the BFA applied.

Figures 17 and 18 present the analysis of underground cavity images at specific depths in the plan view, comparing cases with and without the application of the BFA. The data with the BFA applied, obtained at 3 cm depth intervals, showed a reduced influence from surrounding signals at all depths. As a result, the closed-loop boundaries characteristic of the underground cavities in the plan view became more distinct, and independent region images were formed more clearly.



Figure 17. Comparison of the plan view of cavities at different depths without the BFA: (**a**) 15 cm; (**b**) 18 cm; (**c**) 21 cm; (**d**) 24 cm; (**e**) 27 cm.

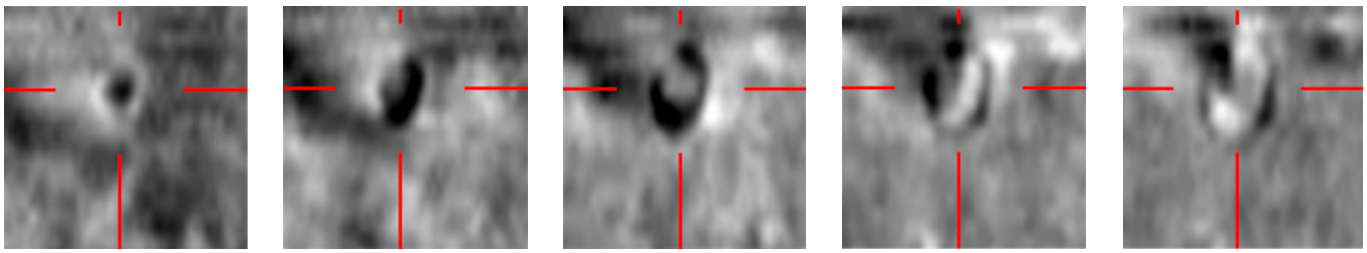
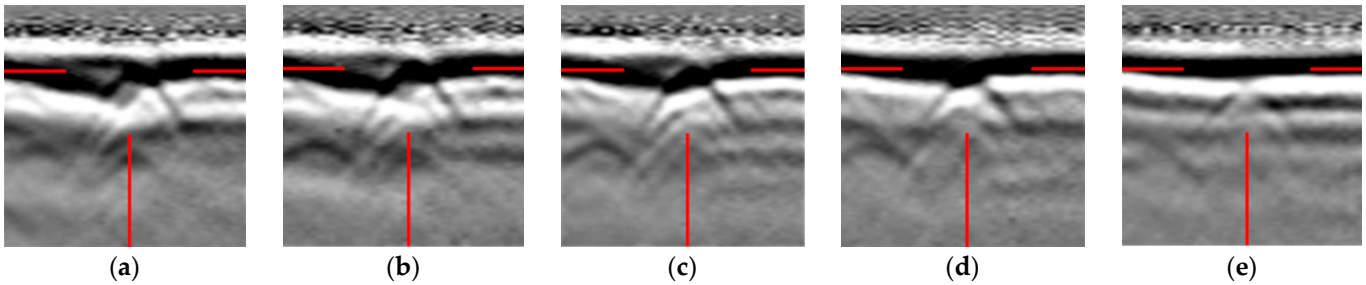


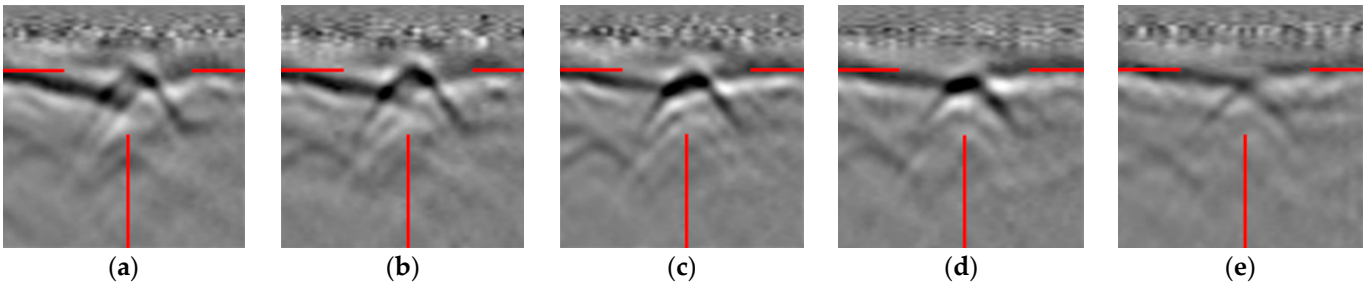
Figure 18. Comparison of the plan view of cavities at different depths with the BFA: (**a**) 15 cm; (**b**) 18 cm; (**c**) 21 cm; (**d**) 24 cm; (**e**) 27 cm.

Figures 19 and 20 show the images of data from five channels where the parabolic shape characteristic of cavities in the longitudinal section is well-visible. These images compare the data without the BFA applied and with the BFA applied. In the five channels, the data without the BFA areis obscured by the black and white straight-line signals representing the boundary characteristics of the asphalt pavement and soil medium. In contrast, the data with the BFA applied clearly show the upper and lower boundary characteristics of the parabolic cavity shape in the longitudinal section, demonstrating that the cavity features are more distinctly detected.



(**a**) (**b**) (**c**) (**d**) (**e**)

Figure 19. Comparison of the longitudinal view of cavities at cChannels without the BFA: (**a**) Channel 5; (**b**) Channel 6; (**c**) Channel 7; (**d**) Channel 8; (**e**) Channel 9.



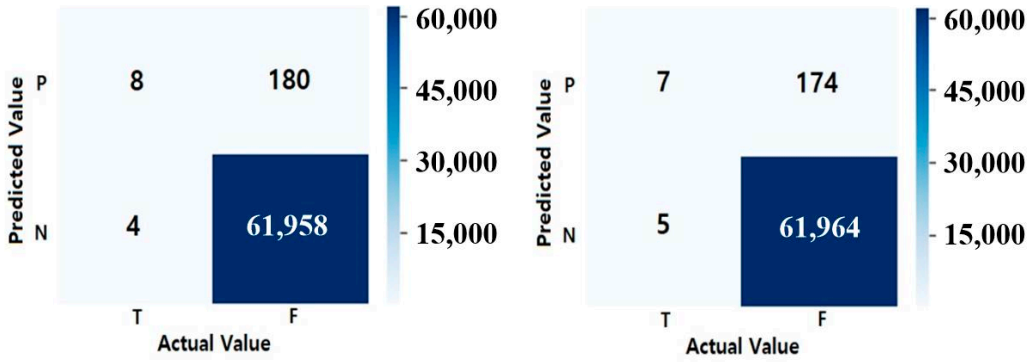
(**a**) (**b**) (**c**) (**d**) (**e**)

Figure 20. Comparison of the longitudinal view of cavities at cChannels with the BFA: (**a**) Channel 5; (**b**) Channel 6; (**c**) Channel 7; (**d**) Channel 8; (**e**) Channel 9.

3.3. Verification of the BFA Effect Using the Pre-Trained C-GAN Model

The 3D GPR data used in the C-GAN model include a total of 12 cavities, with 25 channels, a depth of 2.5 m, and a survey distance of 6215 m. To verify the effect of applying the BFA, tests were conducted and analyzed in two cases: without the BFA and with the BFA applied. Each dataset was input into the pre-trained C-GAN, and it took approximately 22 min to analyze a total distance of 12.4 km.

Assuming the analysis depth is around 80 cm, the 3D GPR data can be viewed as a rectangular prism with dimensions of 25 channels × 0.8 m (depth) × 6215 m (distance). Dividing this rectangular prism into smaller prisms of 5 channels × 0.4 m (depth) × 1 m (distance) results in 62,150 smaller rectangular prisms. The classification results of these 62,150 prisms, when using a confusion matrix, are shown in Figure 21. The x-axis represents the actual values, and the y-axis represents the predicted values. In detail, in the actual value, T is True (Cavity), and F is False (Non-Cavity), while in the predicted value, P is positive (Cavity), and N is Negative (Non-Cavity).



(**a**) (**b**)

Figure 21. Results of the underground object classification: (**a**) aApplication of the BFA; (**b**) nNon-application of the BFA.

Thus, TP and FN indicate the accuracy of the C-GAN model, while TN or FP indicates the prediction failures by the C-GAN model. As an effect of applying BFA, TP and FN increased slightly, but these values are negligible compared to the overall data.

To quantitatively analyze the accuracy of the underground cavity detection results, a comprehensive evaluation index (*F1 Score*) for the fitted characteristic hyperbola was used. This can be calculated as shown in Equations (4)–(6). Here, P is precision, and R is recall. TP, FP, and FN represent true positives, false positives, and false negatives.

$$F1\ Score = \frac{2PR}{P+R} \tag{4}$$

$$P = \frac{TP}{TP+FP} \tag{5}$$

$$R = \frac{TP}{TP+FN} \tag{6}$$

Figure 22 shows the results of the model classification applied to Equations (4)–(6). These results illustrate the impact of the proposed BFA technique on performance through three indicators: F1 score, Precision, and Recall. The high value of false positives affects the F1 score and Precision, resulting in generally some lower values for these metrics. However, both metrics showed higher values when the BFA was applied. Additionally, in a cavity survey, the most crucial aspect is ensuring safety by accurately detecting all cavities. Therefore, Recall, the indicator of how well the C-GAN model predicts actual cavities, is vital. Comparing the Recall values with and without the BFA application, the model with the BFA applied showed higher Recall values by about 15%.

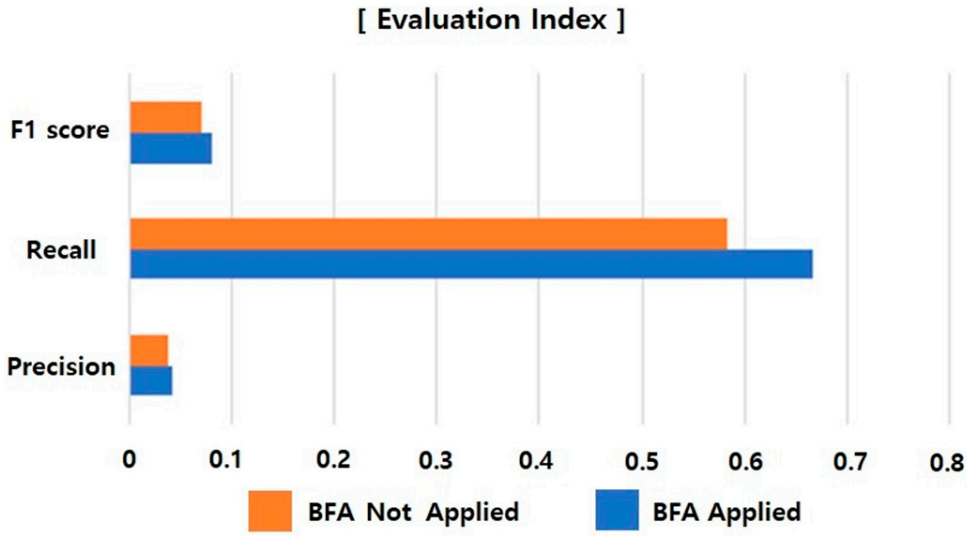


Figure 22. Evaluation index with and without BFA aApplication.

4. Discussion

In this study, a background filtering algorithm (BFA) was developed to enhance the visibility and clarity of underground cavities in a C-GAN model capable of autonomously detecting underground spaces under urban roads using 3D GPR data. A field test was performed by converting 3D GPR data collected in Seoul through the C-GAN model (a deep-learning-based automatic underground cavity detection technique) to which the developed BFA was applied, and the following discussions were derived.

(1) In this study, six steps were performed for the development of the BFA: collecting and converting 3D GPR data, data reconstruction, data alignment, background removal and data interpolation, data amplification, and noise removal using local average subtraction. Subsequently, the BFA was proposed to enhance the visibility of under-

ground cavities by eliminating dominant linear features and unwanted pattern noise in the 3D GPR data. The application of the BFA to the plan view, longitudinal, and cross-sectional views of the cavity locations in the 3D data revealed a clearer detection of the upper and lower boundary characteristics of the parabolic cavity images, which were previously obscured by the boundary characteristics of the asphalt pavement and soil medium.

(2) The C-GAN model, which outputs cavity sections within the underground space based on pre-processed input data and pre-trained learning data from 3D GPR data, eliminates the need for expert concentration or subjective judgment in cavity surveys. Additionally, real-time cavity detection allows for an immediate response to sudden road collapse incidents. The C-GAN model is designed to extract high-level semantic features from scan images, which can be used to train classification networks. Because high-level semantic features contain less interference information, the network model is easier to train and achieves higher recognition rates. Furthermore, the C-GAN-based data enhancement strategy used in this study demonstrates potential for improving the detection accuracy of field data by the network. The C-GAN model demonstrates a higher accuracy rate compared to the CNN model, and its application will significantly aid in predicting ground cavities. Furthermore, by collecting more high-quality training data to enhance the model's learning process and building a comprehensive GPR data library, an improvement in the accuracy of detecting underground structures is also anticipated.

(3) This technology surpasses existing GPR techniques by achieving fast and fully automated data interpretation. The proposed method was experimentally validated using actual 3D GPR data from roads in Seoul. Such data provided a unique opportunity to test the methodology. Although the proposed method demonstrated a satisfactory accuracy in detecting underground cavities, results may vary in different field conditions. Therefore, it is essential to conduct enhanced training processes based on diverse field data, and technological improvements need to be made.

(4) GPR signals reflected from gravel that resemble underground cavities or rocks often cannot be distinguished from actual cavity signals. To overcome these technical limitations, it is necessary to collect higher-quality training data verified through boreholes, enhance learning, and build a robust GPR data library. Additionally, developing further signal processing techniques, such as the phase analysis of reflection waveforms (A-scan), could combine with the current BFA-applied C-GAN architecture to improve the automatic classification accuracy for various types of underground objects, including cavities.

5. Conclusions

This study developed a special algorithm, called a background filtering algorithm (BFA), which can be used in ground cavity detection processes utilizing 3D GPR data. This algorithm enhances the clarity and resolution of GPR data, contributing to the improvement of the quality of data used in the C-GAN model, which is commonly applied in ground cavity detection. It is not a new equipment development or a systemic improvement for finding ground cavities. Rather, it is an economically advantageous technology that can upgrade the existing technology and is considered an excellent innovation due to its shift in approach.

Author Contributions: Conceptualization, D.W.P., H.E.K., K.L. and J.P.; methodology, H.E.K. and J.P.; software, H.E.K.; validation, H.E.K., D.W.P., K.L. and J.P.; formal analysis, K.L. and J.P.; investigation, H.E.K. and J.P.; resources, K.L. and J.P.; data curation, D.W.P. and H.E.K.; writing—original draft preparation, H.E.K. and J.P.; writing—review and editing, D.W.P., K.L. and J.P.; visualization, H.E.K. and K.L.; supervision, J.P.; project administration, K.L. and J.P. All authors have read and agreed to the published version of the manuscript.

Funding: This research received no external funding.

Institutional Review Board Statement: Not applicable.

Informed Consent Statement: Not applicable.

Data Availability Statement: No new data were created or analyzed in this study. Data sharing is not applicable to this article.

Conflicts of Interest: Han Eung Kim was employed by the company Geotechnical Korea Engineering Co., Ltd. The remaining authors declare that the research was conducted in the absence of any commercial or financial relationships that could be construed as a potential conflict of interest.

References

1. Kim, S.M.; Choi, H.; Yoon, J.S.; Park, J.J. A study on the change of cavity area through groundwater injection test under pavement cavity. *J. Soc. Disaster Inf.* **2020**, *16*, 267–275.
2. Park, J.J.; Chung, Y.; Hong, G. A method for cavity scale estimation based on ground-penetrating radar (GPR) explorations: An experimental study. *Adv. Civ. Eng.* **2019**, *1*, 1365759. [CrossRef]
3. Park, J.J.; Kim, I.D. Analysis of the under pavement cavity growth rate using multi-channel GPR equipment. *J. Soc. Disaster Inf.* **2020**, *16*, 60–69.
4. Lee, K.; Kim, D.; Park, J.J. Study on management system of ground sinking based on underground cavity grade. *J. Korean Geosynth. Soc.* **2017**, *16*, 23–33.
5. Han, J.G.; Ryu, Y.S.; Kim, D.; Park, J.J.; Hong, G. A study on expansion and strength characteristics of material for emergency restoration in ground cavity. *J. Korean Geosynth. Soc.* **2017**, *16*, 131–138.
6. Endres, A.L.; Clement, W.P.; Rudolph, D.L. Ground penetrating radar imaging of an aquifer during a pumping test. *Groundwater* **2000**, *38*, 566–576. [CrossRef]
7. Hagrey, A. GPR study of pore water content and salinity in sand. *Geophys. Prospect.* **2000**, *48*, 63–85. [CrossRef]
8. Pyke, K.; Eyuboglu, S.; Daniels, J.J.; Vendl, M. A controlled experiment to determine the water table response using ground penetrating radar. *J. Environ. Eng. Geophys.* **2008**, *13*, 335–342. [CrossRef]
9. Chang, P.; Flatau, A.; Liu, S. Review paper: Health monitoring of civil infrastructure. *Struct. Health Monit.* **2003**, *2*, 257–267. [CrossRef]
10. Nuzzo, L.; Leucci, G.; Negri, S.; Carrozzo, M.T.; Quarta, T. Application of 3D visualization techniques in the analysis of GPR data for archaeology. *Ann. Geophys.* **2002**, *45*, 321–337. [CrossRef]
11. Batayneh, A.; Abdelruhman, A.; Moumani, K. Use of ground-penetrating radar for assessment of potential sinkhole conditions: An example from Ghor al Haditha area. *Environ. Geol.* **2002**, *41*, 977–983.
12. Rodriguez, V.; Gutie'rrez, F.; Green, A.; Carbonel, D.; Horstmeyer, H.; Schmelzbach, C. Characterizing sagging and collapse sinkholes in a Mantled Karst by means of ground penetrating radar (GPR). *Environ. Eng. Geosci.* **2014**, *20*, 109–132. [CrossRef]
13. Conyers, L.B. Analysis and Interpretation of GPR Datasets for Integrated Archaeological Mapping. *Near Surf. Geophys.* **2015**, *13*, 645–651. [CrossRef]
14. Daniels, D.J. *Ground Penetrating Radar*, 2nd ed.; IEE Radar Sonar Navigation and Avionics Series; The Institution of Engineering and Technology: London, UK, 2004.
15. Cassidy, N.J.; Eddies, R.; Dods, S. Void detection beneath reinforced concrete sections: The practical application of ground penetrating radar and ultrasonic techniques. *J. Appl. Geophys.* **2011**, *74*, 263–273. [CrossRef]
16. Lee, S.; Park, J.J.; Cho, B.H. Management of cavities under flexible pavement road network in metropolitan area: Detection, evaluation, and rehabilitation. *Dev. Built Environ.* **2022**, *12*, 100091. [CrossRef]
17. Kim, H.E.; Kim, C.H.; Kim, T.G.; Park, J.J. Verification of ground subsidence risk map based on underground cavity data using DNN technique. *J. Soc. Disaster Inf.* **2023**, *19*, 334–343.
18. Grote, K.; Hubbard, S.; Harvey, J.; Rubin, Y. Evaluation of infiltration in layered pavements using surface GPR reflection techniques. *J. Appl. Geophys.* **2005**, *57*, 129–153. [CrossRef]
19. Annan, A. *Practical Processing of GPR Data*; Sensors & Software: Mississauga, ON, Canada, 1999.
20. Park, B.; Kim, J.; Lee, J.; Kang, M.S.; An, Y.K. Underground object classification for urban roads using instantaneous phase analysis of ground-penetrating radar (GPR) data. *Remote Sens.* **2018**, *10*, 1417. [CrossRef]
21. Al-Nuaimy, W.; Huang, Y.; Nakhkash, M.; Fang, M.T.C.; Nguyen, V.T.; Eriksen, A. Automatic detection of buried utilities and solid objects with GPR using neural networks and pattern recognition. *J. Appl. Geophys.* **2000**, *43*, 157–165. [CrossRef]
22. Gamba, P. Neural detection of pipe signatures in ground penetrating radar images. *IEEE Trans Geosci. Remote Sens.* **2000**, *38*, 790–797. [CrossRef]
23. Zhang, Y.; Huston, D.; Xia, T. Underground object characterization based on neural networks for ground penetrating radar data. In Proceedings of the SPIE, Las Vegas, NV, USA, 21–24 March 2016.
24. Bai, X.; Yang, Y.; Wei, S.; Chen, G.; Li, H.; Li, Y.; Tian, H.; Zhang, T.; Cui, H. A Comprehensive review of conventional and deep learning approaches for Ground-Penetrating Radar detection of raw data. *Appl. Sci.* **2023**, *13*, 7992. [CrossRef]
25. Wang, H.; Ouyang, S.; Liu, Q.; Liao, K.; Zhou, L. Deep-learning-based method for estimating permittivity of Ground-Penetrating Radar targets. *Remote Sens.* **2022**, *14*, 4293. [CrossRef]

26. Xue, W.; Chen, K.; Li, T.; Liu, L.; Zhang, J. Efficient underground target detection of urban roads in Ground-Penetrating Radar images based on neural networks. *Remote Sens.* **2023**, *15*, 1346. [CrossRef]
27. Fang, L.; Yang, F.; Xu, M.; Liu, F. Research on development 3D Ground Penetrating Radar acquisition and control technology for road underground diseases with dual-band antenna arrays. *Sensors* **2023**, *23*, 8301. [CrossRef]

Disclaimer/Publisher's Note: The statements, opinions and data contained in all publications are solely those of the individual author(s) and contributor(s) and not of MDPI and/or the editor(s). MDPI and/or the editor(s) disclaim responsibility for any injury to people or property resulting from any ideas, methods, instructions or products referred to in the content.